# Porous, Functionally-Gradient Pyroelectric Materials

Christopher P Shaw[*], Roger W Whatmore[†‡], Jeffrey R Alcock

School of Industrial and Manufacturing Science,

Cranfield University, Cranfield, Bedfordshire MK43 0AL, UK.

## Abstract

Properties of a new type of pyroelectric ceramic structure containing a layer of known porosity laminated between two dense layers, to form a functionally-gradient material (FGM) are reported. Combination of theoretical models for pyroelectric, dielectric and thermal properties gave a model for the pyroelectric voltage figure of merit ($F_V$) in good agreement with experiment, which had shown a 20% improvement for an introduced central layer porosity of 27%. Preliminary pyroelectric responsivity measurements on FGM infra-red detectors indicated even better improvement. It is postulated that this is due to the porous layer acting as a thermal barrier in the structure.

## Introduction

The piezoelectric and pyroelectric properties of ceramic materials such as those based on lead zirconate titanate (PZT) modified with lead iron niobate (PFN), lead magnesium niobate (PMN)

and various other dopants[1,2], have proved to be useful in many applications to-date. These include such devices as actuators, sensors, sound generators and motors [3], and thermal imaging arrays[4]. In pyroelectric, and many piezoelectric applications, the active material is required in the form of thin (50-300μm) ceramic sheets. In principle, tape casting[5] offers a route to producing such material, either as individual layers which are sintered, or multiple layers which are laminated and sintered to yield the required thicknesses. Recently, large pyroelectric properties within functionally graded materials (FGM) have been reported[6]. The basic idea is to incorporate different layers with differing properties so that the complete structure is optimised for a particular application. In this respect, the lamination of tape cast material offers an ideal route to construct such structures.

Within the present study the aim has been to produce a FGM structure as schematically shown in figure 1, and which consists of a porous layer of pyroelectric material sandwiched between two dense layers of the same material. There has been evidence from the literature that uniformly porous films of PZT have higher pyroelectric responsivities than the dense ones[7]. In addition, the effect on other material properties such as relative permittivity, thermal conductivity and thermal capacitance should have beneficial consequences for a pyroelectric application as long as the pyroelectric coefficient itself is not reduced significantly.

The significance of optimising these properties is highlighted when the figure of merit $(F_v)$[8] is considered:

$$F_v = \frac{p}{c'\varepsilon\varepsilon_0} \qquad\qquad (1)$$

where $\varepsilon_0$ is the permittivity of free space, p is the pyroelectric coefficient, c' is the volume specific heat, and $\varepsilon$ is the relative permittivity of the pyroelectric material.  Obviously, as $F_v$ has been shown to be proportional to the voltage response for pyroelectric detectors it can act as a useful parameter for comparing pyroelectric materials.

**Experimental**

FGMs with a porous central layer were produced via a tape casting process, details of which are given below, followed by the stacking and lamination of several tapes to form the FGM structure. The porosity in the central layer of the FGM was formed by the addition of a sacrificial pore forming agent, corn starch (Sigma-Aldrich, Dorset, UK) to the green tape which would be burnt out during debinding and sintering.  The average particle size of the corn starch used was 15 µm.

FGM samples were prepared by sandwiching either one or two layers of the starch contained tape between a top and bottom layer of starch-free tape.  Consequently, two different dense-porous-dense 'architectures' were produced, which were referred to as, a 1:1:1 layer structure, formed from a tri-layer structure and a 1:2:1 structure formed from a quad-layer.  Only thinner crack-free tapes could be produced for creating the porous central layer, a problem which was thought to have originated from increased drying stresses in the starch-contained tapes compared with the starch-free tapes.  The actual thickness of the  porous layer in these two architectures translated

to approximately 25% and 40% respectively of the total green tape thickness[see Figures 3a and 4a]. In the sintered tapes no microstructural evidence of a boundary between the two original porous layers of the 1:2:1 architecture could be discerned [see Figure 4a].

For the tape casting process, calcined powders, of a doped lead zirconium titanate $(Pb[\{Mg_{1/3}Nb_{2/3})_{0.025}(Zr_{0.825}Ti_{0.175})_{0.975}\}_{0.9927}U_{0.0063}]O_3)$ (PMNZTU) were prepared by a mixed oxide route, as reported previously [9]. Typical primary particle size was 500nm.

Aqueous slips of PMNZTU were produced comprising the powder, a latex binder (Mowilith LDM7651S, Celanese Emulsions, Norden AB, Denmark), a dispersant (Dispex A40, Allied Colloids, Bradford, UK.), and a wetting agent (Surfynol SE-F, Air Products and Chemicals Utrecht, Netherland). The standard composition of a dry, starch free tape is given in Table I. To produce the central layer(s) of the FGMs, green tapes were produced with corn starch contents of 5, 10, 20 and 30 vol% with respect to the powder. In these tapes, the dispersant quantity was kept constant hence the dispersant to powder ratio of the slips increased as the starch content increased.

A combination of stirring and ultrasonic mixing was initially used to combine the PMNZTU, binder, dispersant and water, before ball milling for 4 hours. The starch and surfactants were then added and gently mixed for another hour. Casting was then carried out at a carrier speed of 4.5cm/s, a blade width of 200mm and blade heights of 175μm (starch-free slip) and 100μm (starch-containing slip), onto a Mylar (Richard E. Mistler Inc., Morrisville, PA.) carrier film.

Tapes were allowed to dry at ambient temperatures and humidity, resulting in crack free tapes of dry thickness 116±4µm and 76±7µm for the starch-free and starch contained tapes respectively.

A uniaxial warm press (G.E Moore, Birmingham, UK.) was used to laminate the tape layers into the desired architectures. Three or four layers of 30mm x 30mm squares of tape were stacked between two pieces of silicone coated Mylar, with the silicone coated surfaces presented towards the tape to aid release of the warm pressed structure. The stack was then pressed between two polished steel plates, with a parallel plate configuration, at 50°C for 15mins, at an optimised pressure of 170MPa. The lamination process produced a mean reduction in sample thickness of 20.8% and 22.0% for the 1:1:1 and 1:2:1 sample sets respectively, in comparison to the total thicknesses of the component green tapes.

Debinding and sintering of the samples was carried out using a muffle furnace (PyroTherm, Leicestershire, UK.). Alumina substrates and crucibles which had previously been conditioned with lead (II) oxide (99.9+%, Sigma-Aldrich, Dorset, UK.) were used to help reduce lead loss. For debinding, the samples were placed, uncovered, on flat alumina substrates in the furnace. A debinding profile based on studies by Kristofferson et al.[10] was used: $3°C \, min^{-1}$ to 210°C, hold 15 mins; $1°C \, min^{-1}$ to 320°, hold 15 mins; $1°C \, min^{-1}$ to 500°C, hold 60 mins.

To reduce lead loss from the samples during the sintering stage, small alumina pots containing calcined PMNZTU powder were placed on the alumina substrate around the debound samples. A tightly fitting crucible was used to cover samples and pots. Samples were sintered at 1170°C

for 30 mins.  A ramp rate of 3°C min$^{-1}$ was used on heating and cooling.  A reduction in thickness of between 19.3 and 22.2% was observed on sintering, with the small amount of variation appearing to have no relationship with layer architecture or total starch content of the green tape.  This indicated that the starch induced porosity was not being significantly reduced during the sintering process.

Bulk densities ($\rho_A$) of the sintered samples were determined by using an image analysis system (Q500MC, Leica, Cambridge, UK.) to measure the area of the samples, optical microscopy to determine the FGM thickness and a balance (AT460, Mettler-Toledo Ltd., Leicester, UK.) to record mass. The values of density so-determined were used to calculate the average porosities ($P_A$) for the samples ($P_A=1-\rho_A$). These are presented in Table II. Sintered sample thicknesses varied between the two architectures with mean values of 200µm for 1:1:1 and 234µm for 1:2:1.

SEM images of the cross-sectional fracture surfaces of pieces of the samples were taken to determine grain and porosity data.

For electrical characterisation, Cr/Au electrodes were evaporated onto both sides of the samples. Samples were poled under an electric field of 3kV mm$^{-1}$ using a high voltage source (Alpha II, Brandenburg, Thornton Heath, UK.)  for 10mins in mineral oil at temperatures between 100 - 120°C.  The field was maintained until the oil had been cooled to less than 50°C.  The samples were then placed in an oven at 60 °C for 8 hrs with their electrodes shorted, to remove any space charge introduced by the poling process.

Dielectric measurements were made using an impedance bridge (1689M RLC Digibridge, GenRad Inc., Concord, MA.) at 33Hz with a voltage amplitude of 0.5V. The pyroelectric current response was measured using the Byer-Roundy method[11] on a custom-built computer controlled rig. This used a thermoelectric heater/cooler to apply a thermal saw-tooth profile centred around 25°C, under reduced pressure, whilst reading current data from an electrometer (6517, Keithley Instruments, Cleveland, Ohio). Pyroelectric coefficients were then determined and used to investigate the pyroelectric figure of merit $F_v$.

**Results**

Figures 2a-b show examples of a fracture surface cross section of a sintered starch-free tri-layer FGM. Only small amounts of porosity were observable (corresponding to the experimentally-determined value of 4.2%). No discontinuities corresponding to inter-layer boundaries of the green tape could be distinguished. The average grain size was 5 µm. Figures 3 and 4 show examples of microstructures for the 1:1:1 and 1:2:1 architectures produced from 30% starch tapes in the central layer. The dense regions, figures 3c and 4c, of the FGMs showed an approximate grain size of 5 - 7µm, with grains in the porous regions, figures 3b and 4b, tending to show a smaller value than this, particularly for the grains surrounding individual pores.

Figures 5-8 present the basic electrical properties for both architectures. Data are plotted against the average porosities of the samples. A maximum of 13.2% average porosity was achieved for a 1:2:1 architecture produced from a quad-layer structure with 30% starch content tape as the

central layers.  The minimum porosity content for the layered structures was 4.2% average

porosity, corresponding to a FGM produced with no added starch.

Figure 5 shows the variation in relative permittivity with average porosity for the poled FGM

samples. Poling of the samples had produced about a 17% reduction in relative permittivity down

to the values given in figure 5. Relative permittivity was found to decrease with increasing

porosity at a mean rate of 1.54% per average porosity%. Figure 6 plots the dielectric loss ($\tan\delta$)

against average porosity.  Dielectric loss showed little variation with the porosity at the

frequencies measured.

Figure 7 shows the variation of the average pyroelectric coefficient (determined from heating and

cooling measurement cycles) against the porosity of the samples.  As with relative permittivity,

pyroelectric coefficient decreased with increasing porosity, but at a mean rate of 1.3%/porosity%.

The ratio of pyroelectric coefficient to relative permittivity (measured at 33Hz) is plotted against

porosity in figure 8.  This shows an increase with increasing porosity at a mean rate of

0.5%/porosity% and an improvement in the ratio by a maximum of 5.4% within the 4.2 to 13

percentage porosity range investigated.

**Discussion**

In terms of the desired sintered structure for the porous layers of the FGM samples, it is evident

(from figures 3 and 4) that large pores are distributed evenly throughout the central region. The

choice of 15μm as the original starch particle diameter was an important consideration, as a smaller sized starch particle may have resulted in initial pore sizes which may have been consumed during the sintering stage, as neighbouring grains enlarged. The evidence is that the pore size observed after sintering is between 10-20μm, suggesting that they have originated from isolated starch particles. It is worth pointing out that there is still a level of porosity within the dense layers of the FGM architectures as indicated by the 4.2% level of porosity observed for the starch free trilayer. The visible evidence of this porosity can be seen in figure 2b, for the sintered starch free FGM tape. Here the porosity is situated at the triple points of the grains, an observation reported in previous work[12] for sintered PMNZTU.

As expected, the effect of increasing the porosity has produced a reduction in the values of both ε and p. There is a good deal more scatter in the results from the electrical measurements for the 1:1:1 relative to the 1:2:1 architectures. This may be a consequence of the greater difficulty of "fixing" the porosity in the thinner porous layer during processing, and of being certain about the value of the porosity in these thinner layers. The 1:2:1 materials showed much better consistency.

The proportional reduction in ε has been shown to be greater than p so the p/ε value shows an increase for the porosity range investigated.
In terms of the uniformity of poling across the different layers of the FGM structure, the poling fields dropped across the individual layers should be proportional to the resistivity, and in turn should be proportional to the volume fraction. However, as the poling field was applied for a long time, and was about three times the size of the coercive field for the PMNZTU ferroelectric

material (which is ~10KV/cm), then the small differences in the resistivity should make no difference to the degree of poling in each layer.

The observed effects on the electrical properties can easily be modelled, but first we have to calculate the porosity of the porous layer, from the average porosity and the observed ratio of porous layer thickness $t_L$ to the total ceramic thickness ($T=2t_C+t_L$) – see figure 1. We can put the fractional thickness of the porous layer as $f_L=t_L/T$ ($f_L=0.25$ for the 1:1:1 and 0.4 for the 1:2:1 architectures – see above). Then it is easy to show that the porosity of the porous layer is:

$$P_L = P_C + \frac{1}{f_L}(P_A - P_C) \tag{2}$$

Here, $P_C$ is the porosity of the "dense" ceramic (0.042), and $P_A$ is the measured porosity of the FGM structure as a whole. Similarly, we can calculate the relative permittivity of the porous layer ($\varepsilon_L$) as:

$$\varepsilon_L = \frac{\varepsilon_C \varepsilon_A f_L}{\varepsilon_C - \varepsilon_A(1 - f_L)} \tag{3}$$

Here, $\varepsilon_A$ is the measured dielectric permittivity of the FGM structure as a whole.

The 33Hz relative permittivity data presented in Figure 5 can now be manipulated to give the relative permittivity of the porous layer and then plotted as a function of porous layer relative permittivity. The results are presented in Figure 9, and it can be seen that the $P_L$ values range up to ~0.28. Wersing et al[13] have analysed in some detail the effects of porosity on the relative permittivity of PZT-type ceramics, and have concluded that, of the many different models developed by other workers, the formula presented by Bruggeman[14] gives the best description of the relative permittivity behaviour. For values of $P_L$ up to 0.6, this can be approximated by:

$$\varepsilon_L = \varepsilon_D(1 - \frac{3}{2}P_L) \tag{4}$$

And similarly:

$$\varepsilon_C = \varepsilon_D(1 - \frac{3}{2}P_C) \tag{4a}$$

Where $\varepsilon_D$ is the relative permittivity of a fully-dense ceramic.

The line predicted by the Bruggeman formula is presented in Figure 9 and can be seen to be in excellent agreement with the observations. Using equations (4) and (4a) to replace $\varepsilon_L$ and $\varepsilon_C$ in equation (3) results in equation (5), which predicts the average relative permittivity of a FGM of this type.

$$\varepsilon_A = \frac{\varepsilon_D(1 - \frac{3}{2}P_C)(1 - \frac{3}{2}P_L)}{1 - \frac{3}{2}[f_L P_C + P_L(1 - f_L)]} \tag{5}$$

A full theoretical treatment of the pyroelectric coefficient of a functionally graded bimorph (rather than a trimorph) structure consisting of two layers of pyroelectric ceramic with different dielectric and pyroelectric properties has been presented by Pintille et al[15]. However, this makes several assumptions which are not applicable to the ceramics used here. In particular, their model assumes that there are no mobile charges in the ceramic. In the materials used in this work, the inclusion of the uranium dopant is specifically added to generate low levels of mobile carriers, to reduce the electrical conductivity[2,9]. In this work, the value of the average pyroelectric coefficient ($p_A$) for the functionally-gradient material can be approximated by simply

placing $p_A$ as being proportional to the volume of pyroelectric material between the electrodes ($p_A = p_D(1-P_A)$ where $p_D$ is the pyroelectric coefficient of a fully dense ceramic). The resulting prediction for the variation of $p_A$ is shown as the dashed line in Figure 7. Again, over the range of porosities explored, there is excellent agreement between this simple model and the experimental results. This line is within experimental error of the trend-line obtained by fitting a straight line to all the $p_A$ vs. $P_A$ data.

We now have theoretical models for the relative permittivity and pyroelectric coefficients of the FGM. To get the pyroelectric voltage figure-of-merit, we can model the average volume specific heat as simply being determined by the amount of ceramic in the structure, so that:

$$c'_A = c_P \rho_D (1 - P_A) \tag{6}$$

Where, $c_P$ is the mass specific heat of the ceramic and $\rho_D$ the theoretical density.

A theoretical model can now be presented for the $F_V$ of a FGM pyroelectric ceramic as:

$$F_V^A = \frac{p_D\{1 - \frac{3}{2}[f_L P_C + P_L(1-f_L)]\}}{c_P \rho_D \varepsilon_D \varepsilon_0 (1 - \frac{3}{2}P_C)(1 - \frac{3}{2}P_L)} \tag{7}$$

Figure 10 shows the values of $F_V$ calculated for the FGM using the measured dielectric and pyroelectric properties, and assuming $c'_A$ is determined by equation 6 and using a value of 0.375

Jg$^{-1}$K for $c_P$ as previously-determined for bulk PMNZTU. Also plotted on this figure is a dashed line representing the theoretical prediction from equation 7. There is good agreement between the two. Note that the theoretical prediction line is not a fit of a straight line to the experimental data, but is a first-principles prediction based on the knowledge of the electrical properties of the sintered materials and the experimentally-determined structural properties of the material.

It can be seen that the FGM has a considerably-improved pyroelectric figure-of-merit relative to the uniformly-dense ceramic – a factor of about 20% for the experimentally most-porous FGM relative to a uniform one with 4.2% porosity. Equation 7 can now be used to predict the properties of other structures. It would predict that the most porous structure measured should have had a 31% improvement relative to a fully-dense ceramic of the same composition, while for example, increasing the fractional thickness of the porous layer ($f_L$) to 0.60, while maintaining its porosity at the highest level (27%) should increase the fractional improvement in $F_V$ relative to the dense material by 41%. These would be very useful increases if translated directly into pyroelectric infra-red detector performance.

This work is not the only work to consider the use of porous pyroelectric materials, but it is quite different from previous work. In the earlier work by De Cicco et al[7], a completely different geometry of pyroelectric material was investigated involving buried interdigitated electrodes surrounded by uniformly porous PZT layers, which yielded improvements in figure of merit values when compared with dense bulk PZT. For our FGM's, the dense-porous-dense architecture was advantageous in that dense ceramic skins were needed to facilitate the

conventional surface-electroding used in pyroelectric infra-red detectors. This also conferred strength to the structure.

A further advantage of the structure presented here, in terms of pyroelectric device operation, is that the porous layer should present a thermal barrier to the heat signal entering at the "front" of the device structure, and it is proposed that the use of the dense layers on the outside of the structure should maximise the charge response where the thermal change is at a maximum. Prototype IR sensors were fabricated using examples of FGM ceramics with 1:2:1 architectures and 5% and 30% porosities. The former showed a 1Hz responsivity of $2.5 \times 10^5$ VW$^{-1}$, which is very similar to the average value from the response from a standard device using a conventional ceramic. The device made with higher porosity showed a responsivity of $3.2 \times 10^5$ VW$^{-1}$, which is a useful increase, and at 28 % is rather better than the simple theoretical ratio of figures-of-merit (20%) would have suggested. This could be because the porous layer is forming an intrinsic thermal barrier in the structure and warrants further investigation. It is to be expected, if that were the case, that the improvement would be more-marked at higher modulation frequencies, where the penetration of the thermal wave into the structure would be more-impeded by the porous layer. This represents work in-progress.

**Conclusions**

It has been shown that functionally-graded pyroelectric materials which have a controlled porous layer sandwiched between two dense layers can be made using tape-casting processes employing starch particles as porosity-inducing agents. The dielectric and pyroelectric properties of these

14

materials have been characterised and it has been shown that the inclusion of the porous layer has the effect of reducing average relative permittivity and pyroelectric coefficient, and increasing the $p/\varepsilon$ ratio. Taking the reduction in average volume specific heat into consideration, it has been demonstrated that at least a 20% improvement in the pyroelectric voltage figure of merit can be obtained by inclusion of the thermal layer. Theoretical analysis of the dielectric data has shown that the relative permittivity of the porous layer is very well described by the Bruggeman model and it has been demonstrated that the dependence of the pyroelectric coefficient on the average porosity is well-described by assuming that it is proportional to the volume fraction of pyroelectric material between the electrodes. The models for the pyroelectric, dielectric and heat capacity have been combined to give a model for the voltage figure of merit in terms of the bulk properties and the porosity and thickness of the porous layer. The resulting model shows good agreement with the experimental data and has been used to predict that it should be possible to make FGM pyroelectric ceramics of this type with a 40% improvement in $F_V$. Preliminary experimental measurements on infra-red detectors made using the FGM pyroelectrics have shown an increase in voltage responsivity which is slightly better than that predicted by the simple theory. This could be due to the porous layer acting as a thermal barrier in the structure.

**Acknowledgements**

# References

[1]D, J. Berlincourt, "Piezoelectric Ceramic Compositional Development", Acoust. Soc. Am., 91 3034-3040 (1992).

[2]R. W. Whatmore, "High-Performance, Conducting Pyroelectric Ceramics", Ferroelectrics, 49 [1-4] 201-210 (1983).

[3]R. W. Whatmore, "Ferroelectrics, Microsystems and Nanotechnology", Ferroelectrics, 225 [1-4] 985-998 (1999).

[4]R. W. Whatmore, "Pyroelectric Ceramics and Devices for Thermal Infrared Detection and Imaging", Ferroelectrics,118 241-259 (1991).

[5]J. C. Williams, "Ceramic Fabrication Processes"; pp. 173-98 in Treatise on Material Science and Technology, Vol. 9. Edited by F.F.Y Wang, Academic Press, New York, 1976.

[6]N. W. Schubring, J. V. Mantese, A. L. Micheli, A. B. Catalan and R. J. Lopez, "Charge Pumping and Pseudopyroelectric Effect in Active Ferroelectric Relaxor-Type Films", Phys. Rev. Let., 68 [11] 1778 (1992).

[7]G. De Cicco, B. Morten, D. Dalmonego and M. Prudenziati, "Pyroelectricity of PZT-based Thick-films", Sensors and Actuators, 76 [1-3] 409-415 (1999).

[8]E. H. Putley, "The Pyroelectric Detector"; pp. 259-285 in Semiconductors and Semimetals, Vol. 5, Ch. 6. Edited by R.K Willardson and A.C Beer, Academic Press, New York, 1970.

[9]S. B. Stringfellow, S. Gupta, C. P. Shaw, J. R. Alcock and R. W. Whatmore, "Electrical Conductivity Control in Uranium-Doped $PbZrO_3$–$PbTiO_3$–$Pb(Mg_{1/3}Nb_{2/3})O_3$ Pyroelectric Ceramics ", J. European Ceramic Society, 22 [4] 573-578 (2002).

[10]A. Kristoffersson and E. Carlstrom, "Tape Casting of Alumina in Water with an Acrylic Latex Binder", J. European Ceramic Society, 17 [2-3] 289-297 (1997).

[11]R. L. Byer and C. B. Roundy, "Pyroelectric Coefficient Direct Measurement Technique and Application to a Nsec Response Time Detector", Ferroelectrics, 3 [2-3] 333 (1972).

[12]L. Mortara, A. Navarro, R. W. Whatmore and J. R. Alcock, "Correlation of Sintered Microstructure with Green Density in Thick-Film PZT", pp. 309-12 in Key Engineering Materials,Vol. 264-268, Euro Ceramics VIII Parts 1-3. Edited by H. Mandal and L. Ovecoglu, 2004.  Proceedings of the 8th Conference and Exhibition of the European Ceramic Society, Istanbul, Turkey, 2003. Trans Tech Publications Inc., Zurich.


[13]W. Wersing, K. Lubitz and J. Mohaupt, "Dielectric, Elastic and Piezoelectric Properties of Porous PZT Ceramics", Ferroelectrics, 68 [1-4] 77-97 (1986).

[14]D. A. G. Bruggeman, "Calculating Different Physical Constants of Heterogeneous Substances", Annln. Phys-Leipzig, 24 636 (1935). ("Berechnung Verschiedener Physikalischer Konstanten von Heterogenen Substanzen", Annalen Der Physik).

[15]L. Pintille, I. Pintille and I. Matei, "Equivalent Pyroelectric Coefficient of a Pyroelectric Bimorph Structure", J. Appl. Phys.,88 [12] 7264-7271 (2000).

**Table I.  Composition of the Dried Starch Free Samples**

| Solid Component | Volume (%) |
| --- | --- |
| PMNZTU[a] | 60.1 |
| Dispex A40[b] | 12.2 |
| Latex[c] | 26.1 |
| Surfynol SE-F[d] | 1.6 |

[a]Doped lead zirconium titanate, Cranfield University, UK. [b]Allied Colloids, Bradford, UK. [c]Mowilith LDM7651S, Celanese Emulsions, Norden AB, Denmark. [d]Air Products and Chemicals, Utrecht, Netherland.

**Table II.  Density and porosity of sintered FGM samples**

| Code[a] | Bulk Density (gcm$^{-3}$) | Relative Density (%) | Porosity (%)[b] |
|---|---|---|---|
| FGMA0 | 7.83 | 95.8 | 4.2 |
| FGMA5 | 7.67 | 93.9 | 6.1 |
| FGMA10 | 7.76 | 94.9 | 5.1 |
| FGMA20 | 7.32 | 89.6 | 10.4 |
| FGMA30 | 7.50 | 91.8 | 8.2 |
| | | | |
| FGMB5 | 7.71 | 94.4 | 5.6 |
| FGMB10 | 7.46 | 91.3 | 8.7 |
| FGMB20 | 7.33 | 89.7 | 10.3 |
| FGMB30 | 7.09 | 86.8 | 13.2 |

[a]Code Format:FGMA and FGMB samples have 1:1:1 and 1:2:1 architectures respectively. The number indicates the starch vol.% in the dried green tape used for the middle layer.
[b]Porosity=(100-Relative Density)
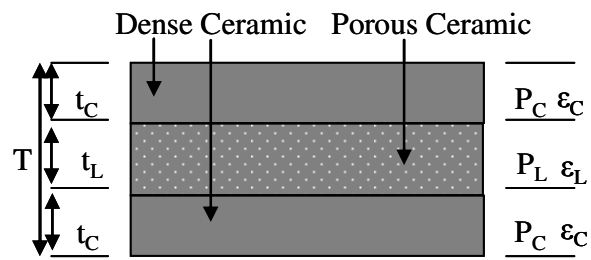
**Fig. 1**. Schematic cross-section of functionally graded pyroelectric ceramic material showing the relative thicknesses(t) of dense and porous layers and their porosities(P) and permittivities($\varepsilon$).
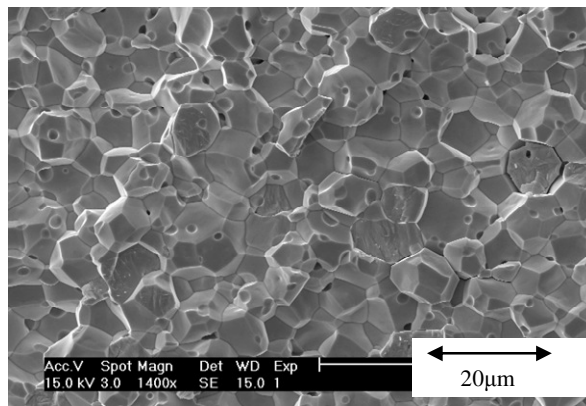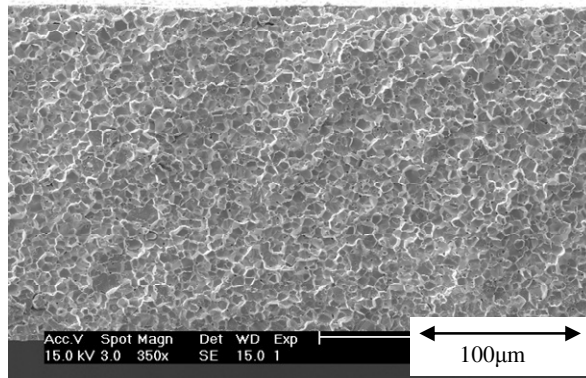
**Fig. 2.** SEM images of a fracture surface of a trilayer sintered PMNZTU material where the center layer had zero added starch (sample FGMAO).
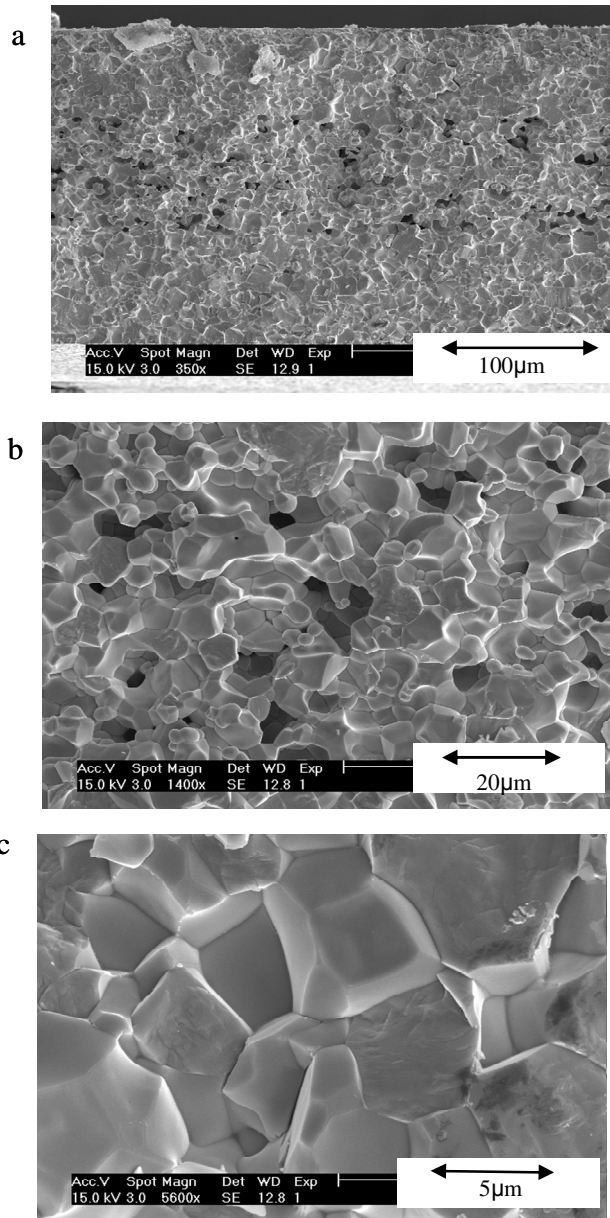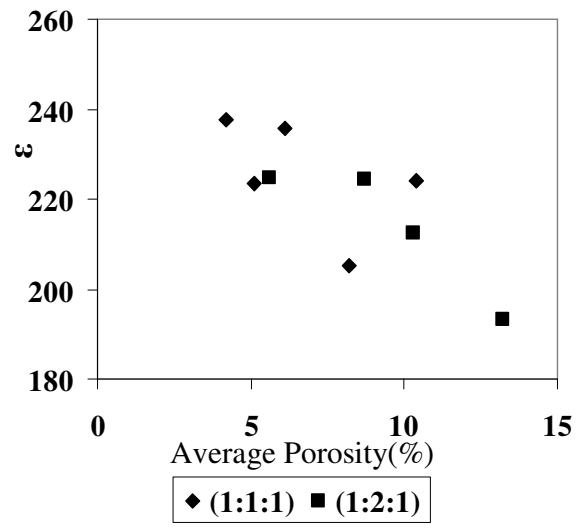
a
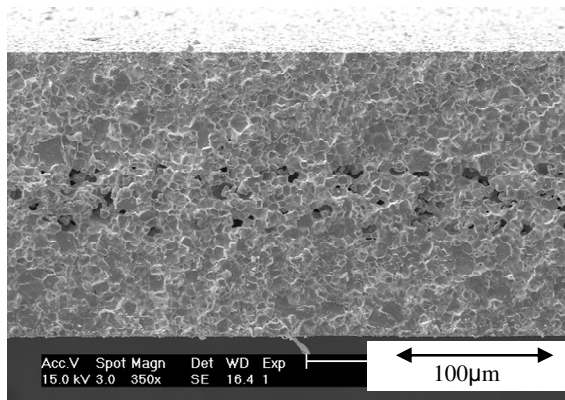


b
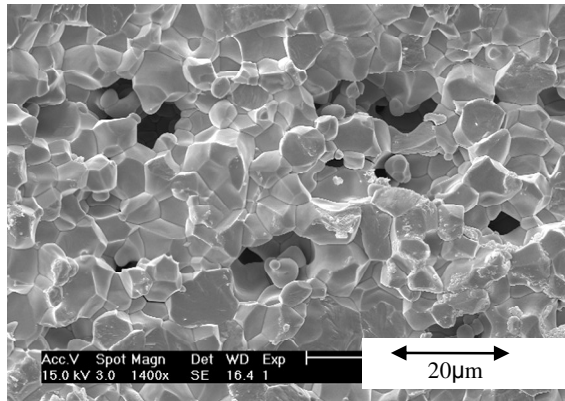


c
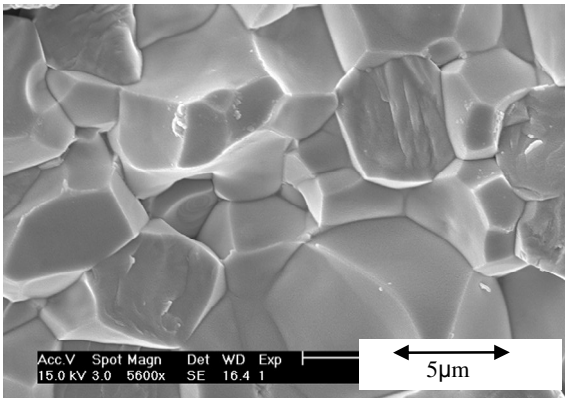


**Fig. 3.** SEM images of fracture surface for sample FGMA30 (a 1:1:1 structure) showing: a) Full cross-section, b) Porous region, and c) Dense region.
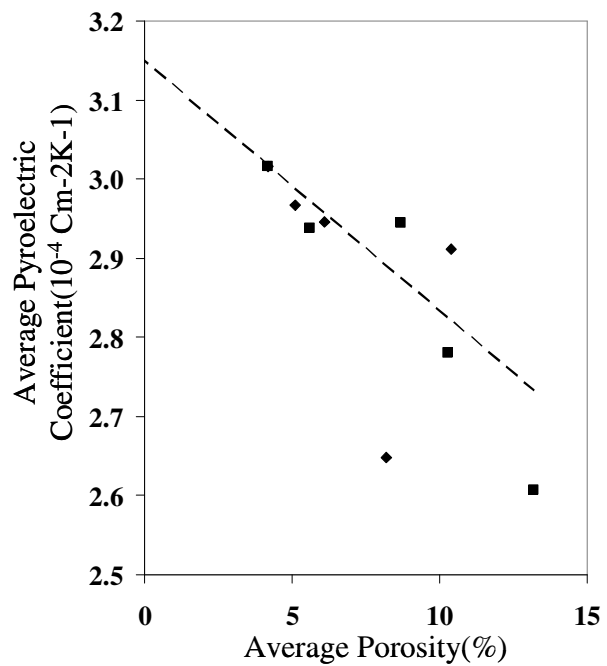
**Fig. 4.** SEM images of fracture surface for sample FGMB30 (a 1:2:1 structure) showing: a) Full cross-section, b) Porous region, and c) Dense region.

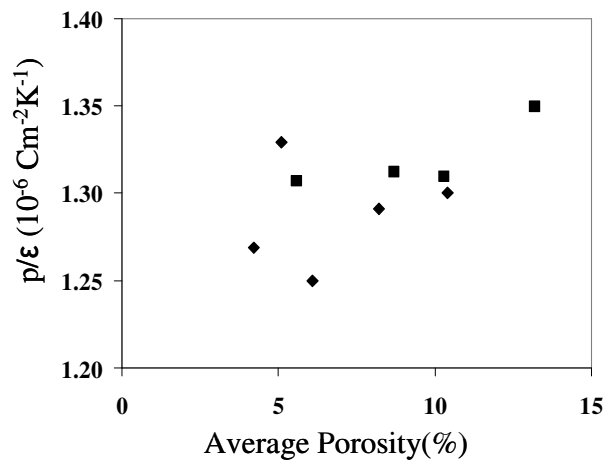**Fig. 5.** Plot of relative permittivity versus average porosity.
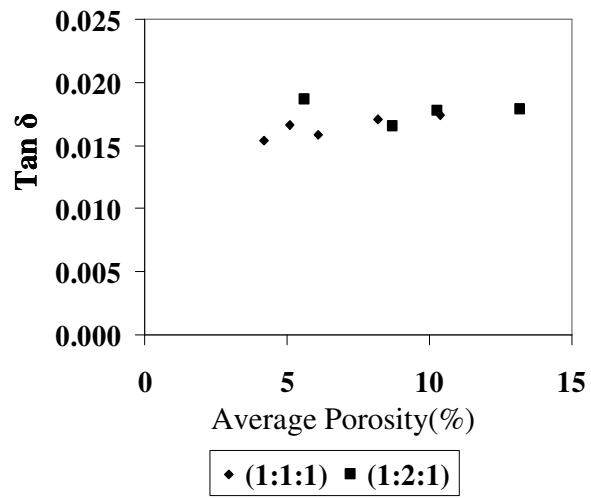
**Fig. 6.** Plot of dielectric loss (Tan δ) versus average porosity.

**Fig. 7.** Plot of average pyroelectric coefficient versus average porosity for the 1:1:1($\blacklozenge$) and 1:2:1($\blacksquare$) samples. The dashed line gives the predicted value of the pyroelectric coefficient assuming that it is simply proportional to the amount of pyroelectric material between the electrodes.

**Fig. 8.** Plot of ρ/ε versus average porosity for the 1:1:1 (♦) and 1:2:1 (■) samples.
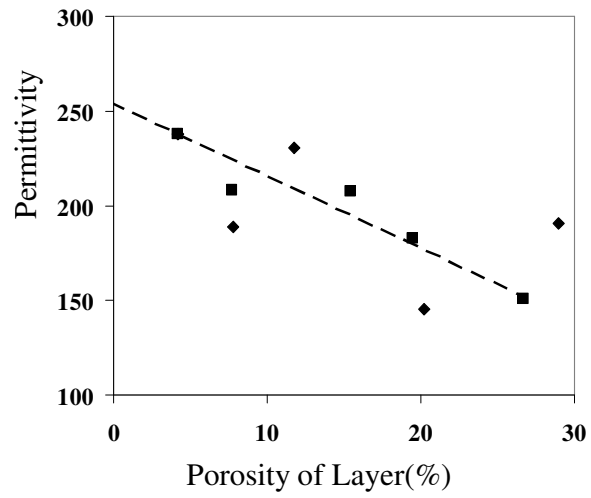
**Fig. 9.** Showing the variation of porous layer relative permittivity with porous layer porosity for the 1:1:1 (♦) and 1:2:1 (■) samples. The dashed line gives the predicted value of relative permittivity with layer porosity according to the Bruggeman formula.
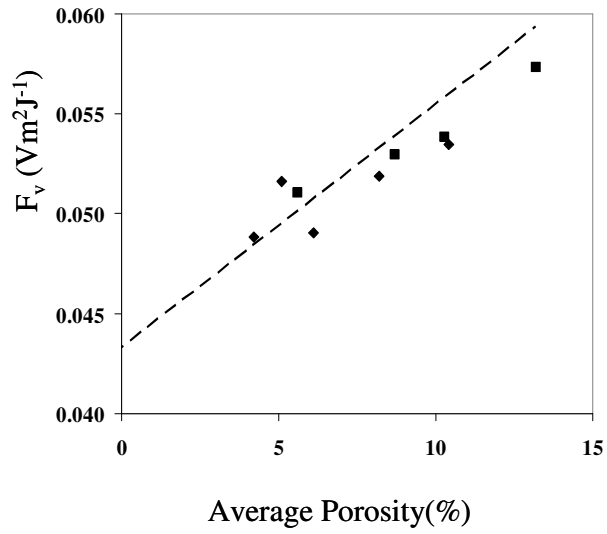
**Fig. 10.** Values of Fv(Voltage Figure of Merit) at 33Hz versus Average Porosity calculated from the data obtained from the 1:1:1 (♦) and 1:2:1 (■) samples. The dashed line represents the prediction from the theoretical model presented in the paper (equation 7).